

1 Size-differentiated Export in Different Dynamical 2 Regimes in the Ocean

3 **M. Dever¹, D. Nicholson¹, M. M. Omand², and A. Mahadevan¹**

4 ¹Woods Hole Oceanographic Institution, Woods Hole, MA 02543, USA

5 ²Graduate School of Oceanography, University of Rhode Island, Narragansett, Rhode Island, USA

6 **Key Points:**

- 7 Submesoscale dynamics enhance the contribution of slow-sinking particles to
8 POC export, especially for steep particle size-spectrum slopes
- 9 Remineralization processes intensify the role of slow-sinking particles, to the
10 point where these particle sometime dominate POC export

11 **Abstract**

12 Export of Particulate Organic Carbon (POC) is mainly driven by gravitational sinking.
 13 Thus, traditionally, it is thought that larger, faster-sinking particles make up most of
 14 the POC export flux. However, this need not be the case in a dynamic oceanic flow
 15 field, where the ocean velocity can influence the descent rate of particles. Particles
 16 with different settling speeds are released in two process-oriented model simulations
 17 of an upper ocean eddying flow to evaluate the impact of (1) ocean dynamics on the
 18 respective contribution of the different sinking-velocity classes to POC export, and (2)
 19 the particle number size-spectrum slope. The analysis reveals that the leading export
 20 mechanism changes from gravitationally-driven to advectively-driven as submesoscale
 21 dynamics become more important. The vertical velocity associated with submesoscale
 22 dynamics enhances the contribution of slower-sinking particles to POC export^{c1}, es-
 23 pecially where the relative abundance of small particles is larger, as captured by a
 24 steeper particle size-spectrum slope. ^{c2}Remineralization ^{c3} generally decreases the
 25 total amount of biomass exported, but its impact is weaker in dynamical regimes where
 26 submesoscale dynamics are present and export is advectively-driven. ^{c4}In an advec-
 27 tively-driven export regime, remineralization processes counter-intuitively enhance the
 28 role of slower-sinking particles to the point where these slower-sinking velocity classes
 29 dominate the export, therefore challenging the traditional paradigm for POC export.
 30 This study demonstrates that slow-sinking particles can be a significant contribution,
 31 and at times, even dominate the export flux.

32 **1 Introduction**

33 Photosynthesis in the sunlit upper ocean and the production of Particulate Or-
 34 ganic Carbon (POC) takes up dissolved inorganic carbon and facilitates the uptake
 35 of CO₂ from the atmosphere. The sinking of POC exports organic carbon from the
 36 upper ocean to the interior, leading to the sequestration of carbon (Falkowski, Barber,
 37 & Smetacek, 1998) on timescales ranging from days to years depending on the sink-
 38 ing depth and circulation. Understanding the mechanisms driving the export of POC
 39 from the ocean's surface to the interior is therefore crucial to better constrain Earth's
 40 carbon budget.

41 Traditionally, POC export is thought to occur through gravitational sinking and
 42 one-dimensional models have been used to describe the sinking POC flux with depth.
 43 Particles produced through primary and secondary production in the surface layer
 44 that are relatively large and fast-sinking, tend to sink out of the upper surface layer
 45 on timescales shorter than the timescale on which the particles get remineralized.
 46 It is reasonable to treat POC export as sinking-dominated if the vertical advective
 47 velocities in the ocean are weaker than the velocities associated with gravitational
 48 sinking. However, Particulate Organic Matter (POM) has a wide range of particle
 49 shape, size and type, that result in particle sinking velocities ranging from practically
 50 zero, to several hundreds of meters per day. The size spectrum, or number distribution
 51 of particle sizes, is usually characterized by a power law with the power ranging between
 52 -2 and -4, for which the abundance of small particles is $\mathcal{O}(10^4 - 10^8)$ greater than large
 53 particles. The biomass size spectrum, which indicates the distribution of biomass vs.
 54 particle size, tends to be flatter and variable in shape (Sheldon, Prakash, & Sutcliffe,
 55 1972) compared to the particle number spectrum, because the volume (and mass) of

^{c1} A steeper particle size spectrum, also increases the relative contribution of smaller, slower-sinking particles

^{c2} Implementing a r

^{c3} scheme

^{c4} Under specific conditions

a particle scales with its linear size raised to a power that exceeds 1 (and typically varies between 2 and 3 depending on shape and porosity). Importantly, it means that a significant fraction of the particulate biomass is in the small size fraction. Even though the sinking velocity w_s of particles does not perfectly relate to particle size l , it is fair to assume that $w_s \sim l^n$ (with $n = 2$ according to Stokes law, and $1 < n < 2$ for complex particle shapes). Due to this, as well as the fact that particles of organic matter are not very much greater in their densities than seawater, a significant fraction of the biomass sinks very slowly (at velocities less than tens of meters per day). When the gravitational sinking velocity of particles is comparable to (or smaller than) the vertical velocities in the flow field, the dynamics of the flow field can impact the trajectories and fate of the POC. Thus, depending on the flow dynamics, and the fraction of slow-sinking particulate biomass, the sinking of organic matter can be affected by the fluid flow in the ocean.

Recent studies have shown that ocean dynamics can play a role in driving the transport of carbon from the euphotic layer to the ocean interior. For example, enhanced vertical velocities along the edge of a mesoscale eddy led to a funneling of particles along the eddy's periphery (van Haren, Millot, & Taupier-Letage, 2006; Waite et al., 2016). Omand et al. (2015) found that submesoscale mixed layer eddies, while contributing to the restratification of a frontal zone, were subducting a large amount of non-sinking POC from the surface productive layer during the onset of the Spring bloom in the subpolar North Atlantic. Advectively subducting plumes or filaments of high oxygen, chlorophyll and small POC (evidenced through backscatter) were detected from a suite of gliders during the North Atlantic Bloom experiment (Alkire et al., 2012). Using model simulations to capture the process of eddy-driven subduction, Omand et al. (2015) estimated the downward advective flux of non-sinking POC and parameterized it. Briggs et al. (2011) quantified the flux of fast-sinking particles consisting largely of diatoms from observations of optical backscatter. But, these estimates did not account for a range of sinking particle velocities. Typically, particulate organic matter (POM) has a wide spectrum of sinking velocities and in order to understand its fate and export, we need to consider the biomass distribution as a function of the particle sinking velocity spectrum and its interaction with the dynamics of the flow field in the ocean.

A growing body of literature focusing on submesoscale (1-10 km) dynamics is exploring its impact on biogeochemical processes (Lévy, Ferrari, Franks, Martin, & Rivière, 2012; Mahadevan, 2016). Submesoscale dynamics, characterized by Rossby numbers of order 1, typically develop in filaments in areas where sharp density fronts exist (Klein & Lapeyre, 2009; McWilliams, 2016; Thomas, Taylor, Ferrari, & Joyce, 2013). In this dynamical regime, geostrophic balance breaks down and a secondary ageostrophic circulation develops across the front, capable of generating large vertical velocities on the order of 100 m/day (Fox-Kemper, Ferrari, & Hallberg, 2008; Mahadevan, 2016). On the denser side of the front, the vorticity is cyclonic and associated with downwelling velocities, while anticyclonic vorticity and upwelling is expected on the lighter side of the front. The distribution of relative vorticity across a front is asymmetric and skewed toward cyclonic vorticity (Rudnick, 2001), leading to more localized and more intense downwelling regions, as opposed to weaker and larger upwelling regions (Mahadevan & Tandon, 2006). Enhanced vertical velocities can generate a local bloom by supplying nutrients to the sunlit layer of the ocean (Lévy, Klein, & Treguier, 2001; Mahadevan & Archer, 2000), or can significantly increase the export of POC to the ocean interior through downwelling (Estapa et al., 2015; Gruber et al., 2011; Lévy et al., 2012; Omand et al., 2015).

The downwelling velocities $\mathcal{O}(100 \text{ m/day})$ generated at submeso-scales provide a physical mechanism capable of competing with gravitational sinking and thus exporting particles over a larger portion of the particle size spectrum. Through this

109 mechanism, smaller particles can be exported on timescales shorter than their rem-
 110 ineralization timescales, despite their slower sinking velocities. Depending on the frac-
 111 tion of biomass in smaller particles (i.e., with slow sinking velocities), the impact of
 112 submesoscale dynamics on the export of POC is potentially significant.

113 In this study, we account for a range of particle sinking velocities in a dynamic
 114 flow field. Despite progress on sampling and viewing particles in the ocean (McDonnell
 115 & Buesseler, 2010), direct measurements of particles sinking velocities are difficult
 116 to obtain, and often inferred from key parameters such as particle type, size, and
 117 density. Though we acknowledge a large variability in these relationships, we assume
 118 a relationship between particle size, biomass, and particle sinking velocity in order to
 119 assess the impact of the flow dynamics and particle size spectrum on the export flux.

120 We rely on a submesoscale-resolving, non-hydrostatic ocean model to simulate the
 121 dynamics in the upper few hundred meters of the ocean. The model does not represent
 122 surface waves or boundary layer turbulence, but rather, examines the fate of particulate
 123 organic matter beneath the turbulent surface boundary layer. The dynamical model
 124 is coupled with a particle-tracking module to model the advection of particles by fluid
 125 flow, while neglecting the effects of particle inertia and drag on their advection. In
 126 addition, the particles sink with a range of sinking velocities (between 0.025–5 m
 127 day⁻¹) ^{c1}scaled from the range of vertical currents modeled in this region. We aim
 128 to address the transitional regime of the particle sinking velocity spectrum, where
 129 both advection and sinking speeds have similar order of magnitudes. This transitional
 130 regime will thus vary depending on the local dynamics: in strong frontal regions such
 131 as western boundary current, vertical currents can $\mathcal{O}(100 \text{ m/day})$.

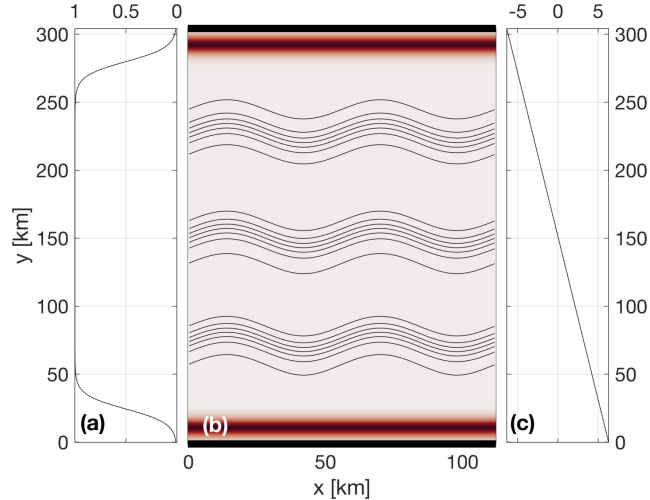
132 The model is used to quantify the contribution of slow-sinking particles to carbon
 133 export, as a function of (1) the dynamics of the flow field, (2) the slope of the sinking
 134 velocity spectrum, and (3) the remineralization timescale. Particles in the model
 135 are prescribed with both a constant and time-varying sinking velocity to mimic a
 136 remineralizing behavior. Particles are released in two fundamentally different flow
 137 fields in terms of dynamics based on observed conditions in the Northeast Pacific:
 138 In the summer, where ocean dynamics are characterized by low Rossby numbers and
 139 weak vertical advective velocities, and in the winter, where ocean dynamics include
 140 submesoscale frontal structures and local Rossby numbers $\mathcal{O}(1)$. Both simulations
 141 and the particle-tracking module are described in Section 2. The impact of particles
 142 characteristics and ocean dynamics on the export of POC is quantified in Section 3,
 143 and discussed in Section 4. Section 5 summarizes the key conclusions of the study.

144 2 Methods

145 2.1 Model setup and domain

146 This study uses a non-hydrostatic, three-dimensional, Process Study Ocean Model
 147 (PSOM; Mahadevan, Olinger, & Street, 1996a, 1996b) to simulate an eddy field that is
 148 representative of the Northeast Pacific Ocean. The model is set in a channel configura-
 149 tion with periodic east-west boundaries, and solid boundaries in the south and north.
 150 The domain covers 112 km in the x-direction, 304 km in the y-direction, and 1000 m
 151 in the vertical (Figure 1). The horizontal resolution is 500 m, while a stretched grid is
 152 used in the vertical with 32 levels ranging in thickness from 1.25 m near the surface to
 153 70 m at the lowermost level. The model is integrated numerically in time and evolves
 154 the temperature, salinity, free-surface height, pressure, and three-dimensional velocity
 155 field from an initial state, subject to momentum and buoyancy fluxes applied through
 156 the surface boundary.

^{c1} Text added.



157 **Figure 1.** PSOM model setup. (a) Meridional profile of scaling coefficient that multiplies the
 158 time-varying zonal wind stress τ_x shown in Fig. 3a. The taper at north and south boundaries
 159 prevents ‘coastal’ up-/down-welling being entirely concentrated in the boundary grid cell. (b)
 160 Restoration factor (color shading) used to dampen internal wave reflection at boundaries as well
 161 as up-/down-welling due to the windstress curl. Surface density contours (black) show the three
 162 fronts used to initialize the model. (c) Meridional variation of the time-dependent surface heat
 163 flux (Fig. 3a) prescribed over the domain.

164 Time-varying wind stress and heat flux are prescribed at the surface boundary.
 165 Time series are computed from measurements collected at Station Papa and available
 166 through the Pacific Marine Environmental Laboratory (PMEL, 2018). Daily wind
 167 stress and net heat fluxes are calculated over the period 2007-2016 to produce a year-
 168 long climatology. A squared low-pass filter with a cut-off frequency of 8.5 days is
 169 applied to both time series to remove high-frequency variability. In all numerical
 170 experiments, simulations are run for the first 5 days without any forcing applied to
 171 the surface boundary. Surface wind stress and heat fluxes are then linearly ramped up
 172 between days 5 and 10 of the simulation, to reach realistic values at day 10.

173 While the meridional component, τ_y , is set to zero, the zonal component of
 174 the wind stress, τ_x , is prescribed at the surface throughout the model domain and
 175 is tapered at the northern and southern boundaries to avoid excessive Ekman-driven
 176 upwelling and downwelling (Figure 1a). A restoration timescale is prescribed to contain
 177 the curl-driven upwelling and downwelling regions generated by the tapering of the
 178 wind stress, as well as to limit internal wave reflection at the solid boundaries back
 179 into the domain (Figure 1b). While net surface heat fluxes are homogeneous in the
 180 zonal direction, a meridional gradient is maintained throughout the simulation. The
 181 meridional gradient was determined from the North American Regional Reanalysis
 182 (NARR) product (Mesinger et al., 2006), and set to $1/24 \text{ W/m}^2/\text{km}$ (Figure 1c).

183 Initial hydrographic conditions are determined from a three-dimensional gridded
 184 field of temperature and salinity from Argo floats (Gaillard, 2015; Gaillard, Reynaud,
 185 Thierry, Kolodziejczyk, & von Schuckmann, 2016). Argo data is averaged monthly
 186 over the period 2002-2012 and two different months are used to initialize the two main
 187 numerical experiments for this study: Climatological conditions in April are used to
 188 initialize the *Papa_summer* experiment, while January climatological conditions are
 189 used to initialize the *Papa_winter* experiment (Table 1). The north-south background

density gradient is then intensified into three fronts located at $y = 75$, $y = 150$, and $y = 225$ km (Figure 1). The amplitude of the density gradient associated with the three fronts is determined from the probability distribution function (PDF) of the density gradients measured by underwater gliders deployed around Station Papa over the period 2008-2010 (Pelland, 2018; Pelland, Eriksen, & Cronin, 2016). To reduce model spin-up time, density fronts are perturbed by a sinusoidal wave with a wavelength close to the 1st baroclinic deformation radius ($\lambda = 66$ km). Similar PSOM configurations were successfully used in previous studies (Mahadevan, D'Asaro, Lee, & Perry, 2012; Omand et al., 2015).

Two main experiments are conducted using the same configuration of PSOM, where only initial conditions and surface forcings are varied: *Papa-summer* aims at generating ocean dynamics representing conditions in the Northeast Pacific in the summertime. Summer ocean dynamics are characterized by a flow generally in geostrophic balance, with relatively weak density gradients and low Rossby numbers ($\ll 1$). *Papa-winter* aims at capturing wintertime ocean conditions in the region. A different dynamical regime is expected to dominate during wintertime when mixed layers are deeper and lateral density gradients enhanced, with sharper density fronts, filament-like features and localized Rossby number $\mathcal{O}(1)$ over spatial scales $\mathcal{O}(1 \text{ km})$ (Callies, Ferrari, Klymak, & Gula, 2015; Mensa et al., 2013; Thompson et al., 2016). The individual characteristics of each of *Papa-summer* and *Papa-winter* are detailed below.

2.1.1 *Papa-summer Model Experiment*

In *Papa-summer*, PSOM is initialized based on climatological Argo data in April. The magnitude of the density gradient across the front is set to $3.34 \times 10^{-6} \text{ kg/m}^3/\text{m}$, which corresponds to the 95th percentile of the PDF of density gradients measured in April from glider data collected in the region (Figure 2 and Table 1). The model is run with a timestep of 216 s and is allowed to spin-up for 60 days, allowing summer stratification to develop. The model is then run for 30 additional days, saving instantaneous model fields every 3 hours for particle tracking. The month of April is chosen for initialization so the experiment would capture the onset of positive net heat fluxes, and the summer restratification that ensues in July-August (Figure 2). In this region, the summer stratification is associated with large primary productivity, particle production, and POC export (e.g., fecal pellets, dead phytoplankton; Plant et al., 2016).

2.1.2 *Papa-winter Model Experiment*

In *Papa-winter*, PSOM is initialized based on climatological Argo data in January. The frontal gradient is set to $3.54 \times 10^{-5} \text{ kg/m}^3/\text{m}$, which corresponds to the 99th percentile of the PDF of density gradients measured in January from glider data collected in the region (Figure 3 and Table 1). The model is allowed to spin-up for 50 days allowing for the prescribed fronts to become unstable. To accommodate for the larger density gradients and stronger velocities, the advective timestep is shortened to 108 s and the horizontal diffusivity is lowered to 0.2 m²/s throughout the experiment. The model is run for 30 additional days, saving instantaneous model fields every 1.5 hours for particle tracking. The month of January is chosen for initialization so the experiment would capture the time of year where the mixed layer is the deepest, and Rossby number $\mathcal{O}(1)$ occur more frequently. The objective is for this experiment to contrast *Papa-summer* by capturing the statistics of ocean conditions dominated by submesoscale dynamics.

224 **Table 1.** Summary of the key characteristics of PSOM experiments *Papa-summer* and
 225 *Papa-winter*.

	<i>Papa-summer</i>	<i>Papa-winter</i>
Time period	April – July	January – March
Spin-up	60 days	50 days
Advective timestep	216 s	108 s
Horizontal diffusivity	1 m ² s ⁻¹	0.2 m ² s ⁻¹
Restoration timescale	3 days	15 days
Zonal wind stress	0 – +0.16 N m ⁻²	-0.05 – +0.17 N m ⁻²
Surface heat flux	-46.8 – +167.5 W m ⁻²	-57.6 – +15.3 W m ⁻²
Maximum M ² ($\times 10^{-8}$)		
initial	3.2 s ⁻²	33.9 s ⁻²
spun-up	12.0 s ⁻²	50.0 s ⁻²
Maximum N ² ($\times 10^{-4}$)		
initial	1.5 s ⁻²	1.6 s ⁻²
spun-up	3.1 s ⁻²	1.1 s ⁻²
Averaged mixed layer depth		
initial	73 m	85 m
spun-up	11 m	93 m

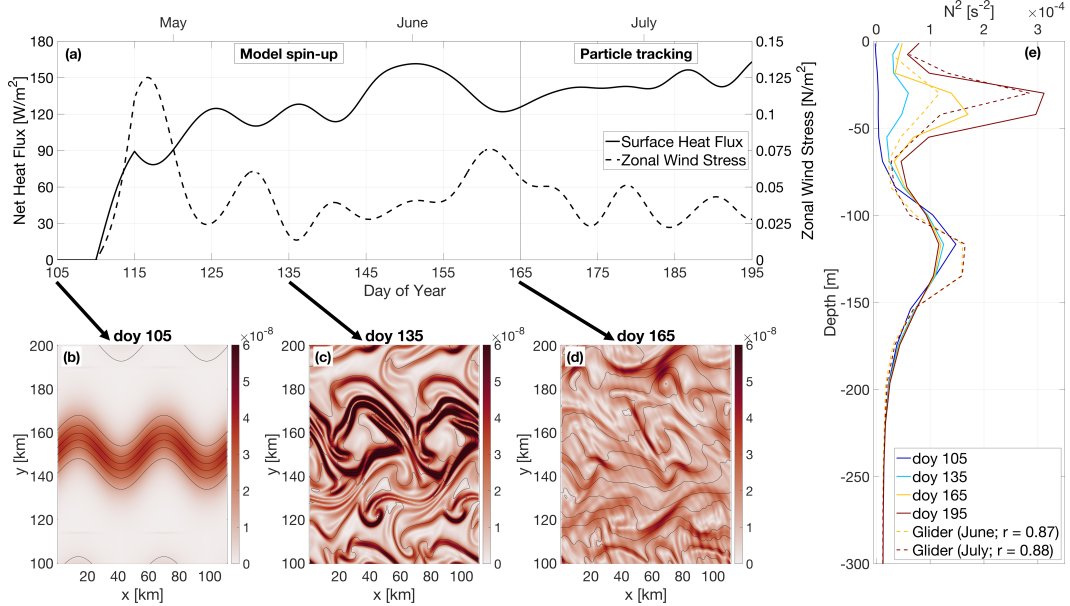
2.1.3 Validation

To ensure that PSOM simulations yielded realistic conditions for both *Papa-summer* and *Papa-winter*, distributions of horizontal (M^2) and vertical (N^2) buoyancy gradients are compared with glider observations collected over the period 2008-2009 (Pelland et al., 2016). During this period, underwater gliders sampled in a “bow-tie” pattern centered on Station Papa. Gliders sample the water column in a triangular wave pattern, whose shape is easily affected by currents, due to the slow moving speed of the glider (~1 km/hr). It is therefore challenging to associate a specific spatial scale with gradients computed between glider profiles, as profile separation distances can be highly variable through depth and time. To circumvent this issue, horizontal buoyancy gradients are computed between each pair of glider profiles available within one branch of the bow-tie. Each along-track lateral buoyancy gradient is thus associated with a specific separation scale and a timestamp. Glider-based density gradients can be affected by internal waves. To filter the impact of internal waves on the PDF of horizontal buoyancy gradients, only gradients computed at a scale of twice the Rossby radius ± 1 km are considered. Rossby radii are estimated from the glider data and are ~ 8 km in winter and ~ 20 km in summer.

2.2 Particle Tracking Experiments

2.2.1 Particle Advection Scheme

To quantify the impact of submesoscale dynamics on the export of Particulate Organic Matter (POC), Lagrangian particle trajectories are computed using the same scheme as in “TRACMASS” (Döös, Kjellsson, & Jönsson, 2013) with the flow fields from the two experiments described above. The three-dimensional, non-divergent velocity components from the faces of each “C” grid cell are linearly interpolated onto the particle’s position within the grid cell. For example, the eastward (along the x-axis)



226 **Figure 2.** PSOM configuration for *Papa_summer*. (a) Time series of net heat fluxes and wind
 227 stress prescribed at the surface. Notice the positive heat fluxes, as well as downfront winds (i.e.
 228 eastward) persisting throughout the experiment. (b)-(d) surface horizontal buoyancy gradients
 229 $M^2 = |\nabla_H b|^2$ (in s^{-2}) at day of year (doy) 105, 135, and 165. Black contours show isopycnals (in
 230 kg/m³; CI = 0.01 kg/m³). (e) Vertical profile of the buoyancy frequency N^2 at day of year 105,
 231 135, 165, and 195, showing the development of summer stratification centered at $z = 30$ m (solid
 232 lines). Monthly-average vertical stratification obtained from glider profiles collected in June and
 233 July are superimposed (dashed lines), along with the correlation coefficient between observations
 234 and model outputs.

velocity of a particle is given by

$$u(x) = u_{i-1} + \frac{(x - x_{i-1})}{(x_i - x_{i-1})} (u_i - u_{i-1}), \quad (1)$$

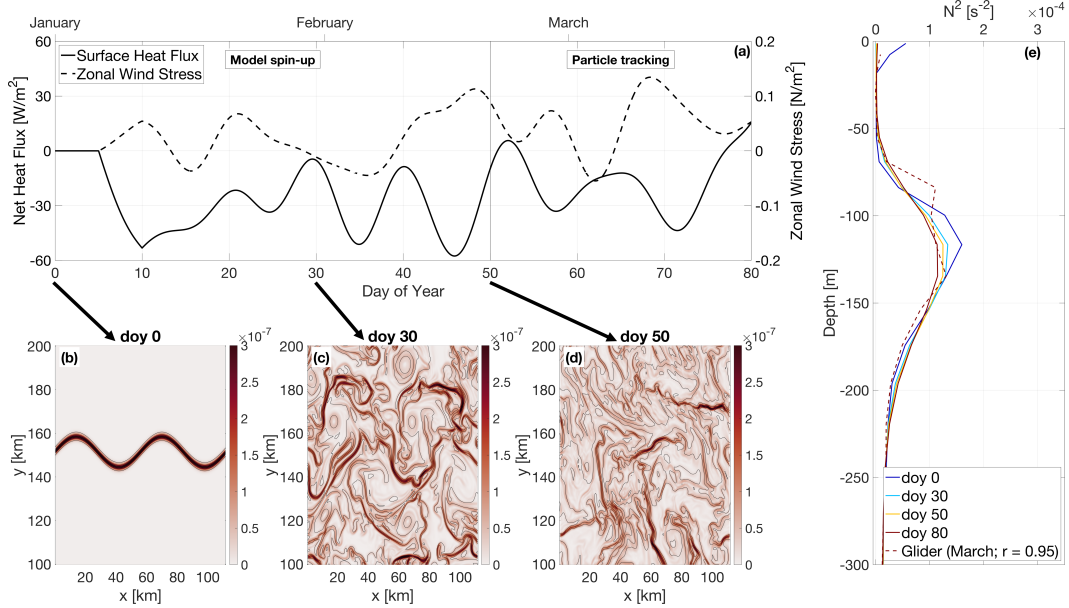
where the subscripts $i - 1$ and i denote the western and eastern walls of the grid cell where the particle is located, respectively. This can be re-written as

$$\frac{\partial x}{\partial t} + \beta x + \delta = 0, \quad (2)$$

where $\beta = (u_i - u_{i-1})/\Delta x$ and $\delta = -u_{i-1} - \beta x_{i-1}$ (Döös et al., 2013). This differential equation can be solved analytically for $\beta \neq 0$ as

$$x_{t_1} = \left(x_0 + \frac{\delta}{\beta} \right) \exp^{-\beta(t_1 - t_0)} - \frac{\delta}{\beta} \quad (3)$$

The time it will take for the particle to reach the eastern or western face of the grid cell can be computed by taking $x_{t_1} = x_i$ or $x_{t_1} = x_{i-1}$, respectively, and solving for t_1 . For each advective timestep, the times required for the particle to reach any of the 6 walls of the grid cell are computed using (3). If any of those times is shorter than the advective timestep, the particle is advected until it reaches the cell wall. Then the flow field in the adjacent grid cell is considered and the particle is advected over the remaining time.



249 **Figure 3.** PSOM configuration for *Papa_winter*. (a) time series of net heat fluxes and wind
 250 stress prescribed at the surface. Notice the mostly negative heat fluxes, as well as alternating
 251 zonal wind direction. (b)-(d) surface horizontal buoyancy gradients $M^2 = |\nabla_H b|^2$ (in s^{-2}) at day
 252 of year (doy) 0, 30, and 50. Black contours show isopycnals (in kg/m^3 ; CI = $0.01\ kg/m^3$). (e)
 253 Vertical profile of the buoyancy frequency N^2 at doy 0, 30, 50, and 80, showing the persistence
 254 of the halocline between $z = 80$ and $z = 180$ m throughout the experiment (solid lines). Monthly-
 255 average vertical stratification obtained from glider profiles collected in March is superimposed
 256 (dashed line), along with the correlation coefficient between observations and model outputs.

283 2.2.2 Particle Seeding

284 For all particle-tracking experiments, a single particle seeding event is prescribed.
 285 In the horizontal, particles are seeded every 250 m over the entire domain in the x-
 286 direction, and for $100 < y < 200$ km in the y-direction. The seeding is centered over
 287 the mean position of the central front (see Figure 2) and is therefore not affected by
 288 undesired effects created by the solid north-south solid boundaries. In the vertical,
 289 particles are seeded every 1 m between 75 and 85 m. This depth range is chosen as it
 290 corresponds to the average euphotic depth at Station Papa, defined by the 1% light
 291 level. ^{c1}Particle seeding is located at the base of the euphotic layer where biological
 292 processes not captured by the particles (e.g., grazing, repackaging, aggregation,
 293 etc.) are not as active (Ducklow, Steinberg, & Buesseler, 2001). The euphotic depth
 294 was computed for the months of February and June over the period 2007-2016 from
 295 profiles of Photosynthetically ^{c2}Active Radiation (PAR) collected at Station Papa as
 296 part of the long-term monitoring of Line P executed by the Department of Fisheries
 297 and Ocean Canada^{c2}. The average euphotic depth computed for both of these months
 298 is around 80 m, which agrees with previously established estimates of the euphotic
 299 depth (Harrison, Whitney, Tsuda, Saito, & Tadokoro, 2004; Sherry, Boyd, Sugimoto,
 300 & Harrison, 1999).

^{c1} *Text added.*

^{c2} *Available*

^{c2} <https://www.waterproperties.ca/linep/index.php>

In each particle-tracking experiment, four different classes of particles are released. Each particle class is characterized by a different sinking velocity: 0.025, ^{c1}1, and 5 m/day. ^{c2}In this study, these particle classes are referred to as slow-, intermediate-, and fast-sinking particles. This characterization is not based on the absolute value of the sinking rate, but rather on the ratio with vertical currents in the study region. While 5 m/day remains a relatively slow sinking rate, the slowest-sinking class is essentially selected to represent non-sinking particles: based on the setup of our experiments, the slowest-sinking particles would take 800 days on average to be exported to a depth of 100 m through gravitational sinking, a timescale much greater than commonly observed remineralization timescales. The fastest-sinking velocity is chosen as an end-member velocity class of particle^{c3}, based on the PDF of vertical velocities in the model. At any given time, at least 85% of the model vertical velocity is weaker than 5 m/day. The results presented for the 5 m/day sinking class can therefore be theoretically extrapolated to any class with a higher sinking velocity.

The advective timestep for particles is set to 1.5 hours. The flow field is linearly interpolated in time between model outputs, justifying the higher temporal resolution used for particle tracking in *Papa_winter*. Particle positions are saved every 3 hours, along with key model variables interpolated onto the particle positions (e.g., density, vorticity). Particles are tracked for ^{c1}four weeks (28 days). Each particle-tracking experiment contains 1,971,717 particles per sinking-velocity class, for a total of 9,858,585 particles. Particles located deeper than the maximum winter mixed layer (i.e., 100 m; Pelland et al., 2016; Plant et al., 2016) are considered exported, as they will likely not be re-entrained into the mixed layer.

2.2.3 Density and Biomass Spectra

The slope ξ of the size spectrum of particles (also known as the Junge slope; White et al., 2015) is the slope of the log-log curve of particle number N vs. particle radius r , where

$$N(r) = N_0 \left(\frac{r}{r_0} \right)^{-\xi}. \quad (4)$$

Here, N_0 and r_0 represent a reference particle number and radius, chosen arbitrarily. For small particles ($<400 \mu\text{m}$) and relatively low temperature ($<15^\circ\text{C}$), it has been shown that the relationship between particle radius r and sinking velocity w_s exhibits a range of variation and is difficult to determine empirically. Nevertheless, Stokes' law, where $w_s \propto r^2$, is often used as a lower-bound sinking velocity estimate (Bach et al., 2012).

Assuming a Stokes-like relationship, we can construct a particle sinking velocity spectrum $N(w_s)$ based on (4), as

$$N(w_s) = N_0 \left(\frac{w_s}{w_{s0}} \right)^{-\xi/2}, \quad (5)$$

where w_{s0} is the sinking speed of particles with radius r_0 . For a specific slope and sinking-velocity class, an equivalent number of particles per simulated particle can be computed using (5) (See Figure 4). For example, using the largest sinking velocity class as a reference (i.e., $w_{s0} = 5 \text{ m/day}$ and $N_0 = 1,971,717$), and a spectral slope $\xi = 4$, each simulated particle with a sinking velocity of 0.025 m/day in fact represents 40,000 particles (Figure 4). The relative biomass of a particle in a specific sinking-velocity class, $B_p(w_s)$ can be estimated if the biomass is assumed to scale with the

^{c1} 0.05,

^{c2} Text added.

^{c3} that will be exported in its entirety over the course of our experiment.

^{c1} three

particle's volume. The relative biomass of one particle in a sinking-velocity class w_s can therefore be computed as

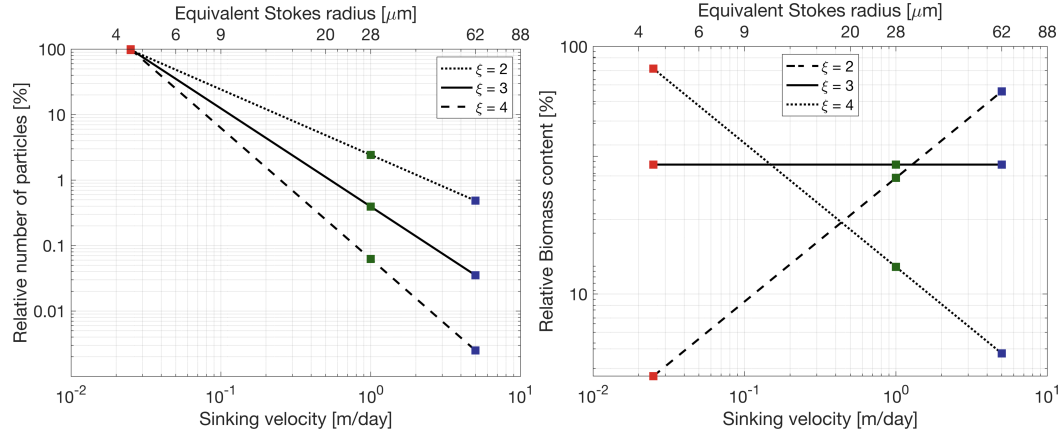


Figure 4. Relative number of particles (left) and biomass (right) as a function of sinking velocity w_s . Sinking velocity spectrum are shown for three different Junge slope ξ : 2 (dotted), 3 (solid), and 2 (dashed). Colored squares indicate the sinking velocities of the three particle classes modeled: 0.025 m/day (red), 1 m/day (green), and 5 m/day (blue).

$$B_p(w_s) = B_p(w_{s_0}) \left(\frac{w_s}{w_{s_0}} \right)^{3/2} \quad (6)$$

where $B_p(w_{s_0})$ is the biomass of a particle in the sinking velocity class w_{s_0} . The total biomass associated with one simulated particle can be obtained by scaling (6) by the ratio $N(w_s)/N_0$:

$$B(w_s) = B_0 \left(\frac{w_s}{w_{s_0}} \right)^{3/2} \frac{N(w_s)}{N_0} \quad (7)$$

where $B_0 = B_p(w_{s_0})$. Combining (5) and (7) yields an expression relating the biomass associated with a simulated particle for a specific sinking-velocity class and the spectral slope (Figure 4):

$$B(w_s) = B_0 \left(\frac{w_s}{w_{s_0}} \right)^{\frac{3-\xi}{2}}. \quad (8)$$

Using the same example as before where $\xi = 4$, if the amount of biomass associated with one simulated particle in the 5 m/day sinking-velocity class is taken as $B_0 = 1$, then one simulated particle sinking at 0.025 m/day contains 14.14 units of biomass and a single particle contains $14.14/40,000 = 3.5 \times 10^{-4}$ units of biomass (see Figure 4). This normalized formulation of particle number and biomass (see Equations (5) and (8)) has the advantage that the impact of spectral slope on the relative export of biomass can be quantified without needing a large number of particle-tracking experiments, where the number of seeded particles would vary to account for the different spectral slopes. For the purpose of this study, only the relative amount of biomass is relevant. For simplicity, we define a normalized biomass unit for $\xi = 3$ as $B_0 = 1$. The values taken by B_0 for other Junge slopes ξ are computed under the condition that the total amount of biomass is kept constant (Figure 4b).

2.2.4 Particle Remineralization Scheme

Remineralization of particles as they sink through the water column impacts the amount of biomass exported. Slow-sinking particles generally contain less biomass

and spend more time in the mixed layer, which means that they are remineralized at a shallower depth than faster sinking particles. Remineralization processes are complex, species-dependent, and generally not well-understood. In the absence of a consensus on a general functional form of particle remineralization, we rely on an idealized relationship which assumes that the biomass content of a particle decreases in time proportionally to the particle volume. Remineralization is thus modeled as an exponential decrease of biomass with time at a rate k (Iversen & Ploug, 2010, 2013)

$$B(t) = B^0 \exp(-kt), \quad (9)$$

where B^0 denotes the biomass content at $t = 0$ days, and the remineralization rate is taken to be $k = 0.13 \text{ day}^{-1}$ in this study (Iversen & Ploug, 2010). This remineralization rate is independent of particle sinking velocity, and seems to lie within the range of other estimates (Iversen & Ploug, 2010, 2013; Ploug, Iversen, Koski, & Buitenhuis, 2008). The change in biomass with time is in turn expected to affect the sinking velocity of the particle. Given that $B \propto w^{3/2}$ (see Equation (6)), particles in all sinking-velocity classes undergo a decay in sinking speed according to

$$w_s(t) = w_s^0 \exp\left(-\frac{2kt}{3}\right), \quad (10)$$

where w_s^0 is the initial sinking velocity at $t = 0$ days. In this study, the impact of remineralization is thus considered through the implementation of a time-dependent sinking velocity (Equation 10). While particles classes are classified based on their initial sinking-velocity, it is worth noting that over the length of the particle-tracking experiments that include remineralization (28 days), particle sinking speeds slow down to 10% of their initial velocity.

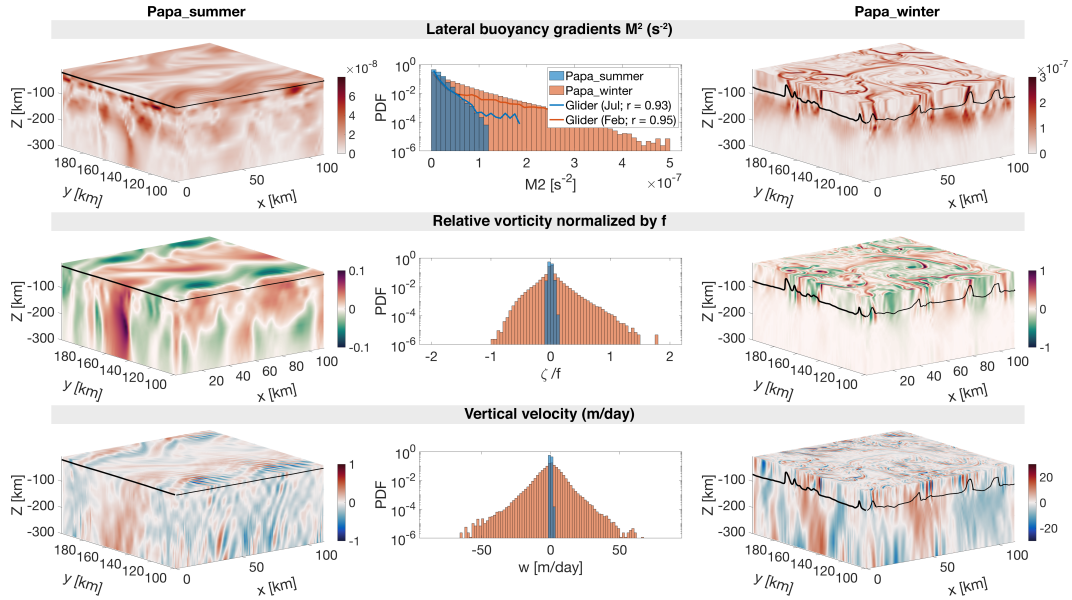
3 Results

3.1 Seasonally varying dynamical regimes

Two model experiments are designed to capture different dynamical conditions observed in the Northeast Pacific Ocean in summer and winter. *Papa_summer* is initialized in early spring (doy 105) when the water column is characterized by a relatively deep mixed layer (~ 100 m) and a halocline located between 100 and 150 m (Figure 2). The forcing by a realistic, positive, net heat flux generates the restratification of the water column, with the development of a strong thermocline between 25 and 50 m leading to the shoaling of the mixed layer and a subsurface peak in N^2 at about 30 m (see Figure 2). A comparison between model outputs and monthly-averaged density profiles from underwater gliders collected in June and July over the period 2008-2009 yields correlation coefficients of $r = 0.87$ and $r = 0.88$, respectively. These high correlation suggest that *Papa_summer* numerical experiment captures the vertical spring and summer conditions in the Northeast Pacific Ocean.

In the horizontal, the prescribed density fronts progressively become unstable within the first 60 days of the experiment (Figure 2). During this time, the Total Kinetic Energy (KE_{tot}) contained in the model domain slowly increases before reaching a maximum at doy 162, where it remains relatively constant for the rest of the simulation. The flattening of the KE_{tot} curve is used to determine the time necessary for the simulation to spin-up, hence determining the start day of the particle-tracking experiments. The ocean dynamics associated with *Papa_summer* are characterized using PDFs of horizontal buoyancy gradients ($M^2 = |\nabla_H b|^2$), vertical velocities (w), and Rossby numbers computed from the normalized vertical component of the relative vorticity ($\text{Ro} = (v_x - u_y)/f$ where $f = 1.12 \times 10^{-4}$; Figure 5).

Lateral buoyancy gradients in the summer are relatively weak $\mathcal{O}(10^{-8} \text{ s}^{-2})$ and result in low Rossby numbers $\mathcal{O}(0.1)$, with positive relative vorticity on the denser



378 **Figure 5.** Snapshots of M^2 (top), ζ/f (middle), and w (bottom) half-way through the
 379 particle tracking experiment for *Papa_summer* (left) and *Papa_winter* (right), with the Mixed Layer
 380 Depth indicated by the solid black line. The corresponding Probability Distribution Functions
 381 (PDFs) are shown in the center for both *Papa_summer* (blue) and *Papa_winter* (red). Note the
 382 different colorbars used for *Papa_summer* and *Papa_winter*. Histograms of M^2 computed from
 383 glider data at Station Papa in February (blue line) and July (red line) are superimposed in the
 384 top middle panel.

387 (north) side of the front and negative relative vorticity on the lighter (south) side
 388 of the front. Corresponding vertical velocities are consistently weaker than 1 m/day
 389 ($<10^{-5}$ m/s) and are characterized by regions of weak upwelling and downwelling on
 390 10 km scales, associated with the meandering of the front (Bower & Rossby, 1989).
 391 Alternating bands of upwelling and downwelling at $\mathcal{O}(1 \text{ km})$ spatial scale are super-
 392 imposed, and likely caused by propagating internal waves. Coherent vertical velocities
 393 structures extend to depths much greater than the mixed layer depth ($\sim 25 \text{ m}$; Figure
 394 5). The amplitude of the vertical velocity field coincides with the expected order of
 395 magnitude given by the scaling $w \propto Ro f U / N$ (Mahadevan, 2016): using $Ro \sim 0.1$
 396 (Figure 5), $N \sim 10^{-2} \text{ s}^{-1}$ (Figure 2), $f \sim 10^{-5} \text{ s}^{-1}$, and $U \sim 0.01 \text{ m/s}$, we obtain
 397 $w \sim 10^{-6} \text{ m/s}$, or $\sim 10^{-1} \text{ m/day}$.

398 *Papa_winter* is, on the other hand, initialized in the winter (doy 0) to capture a
 399 time period where the mixed layer depth is deeper ($\sim 100 \text{ m}$) and density gradients
 400 more pronounced (Pelland et al., 2016). At this time of year, the water column in
 401 this region is characterized by the presence of a deep halocline between 100 and 150
 402 m (Figure 3 Pelland et al., 2016). After spin-up, the vertical stratification remains
 403 consistent throughout the model run, and compares well with the vertical profile ob-
 404 tained from glider observations for the month of March ($r = 0.95$; see Figure 3). In
 405 the horizontal, prescribed density fronts are much sharper than in summer (i.e., over
 406 smaller spatial scales $\mathcal{O}(1 \text{ km})$ vs. $\mathcal{O}(10 \text{ km})$). Because of these stronger density
 407 gradients, combined with the alternating zonal winds and constantly negative surface
 408 heat flux, the fronts become unstable more rapidly than in summer (Figure 3). As a
 409 result, KE_{tot} starts to plateau at doy 48. The experiment is considered spun-up by
 410 doy 50 and the particle-tracking experiment is initialized.

The frontal structures visible in the horizontal buoyancy gradient field are associated with filaments of relatively high Rossby number of $\mathcal{O}(1)$ (Figure 5). The PDF of relative vorticity reveals a positively-skewed distribution ($s = 0.68$). This is in agreement with the fact that the relative vorticity is more likely to be cyclonic than anticyclonic, based on conservation of potential vorticity (Hoskins & Bretherton, 1972). Regions with high Rossby number are localized and located in the mixed layer exclusively. In places where the local Rossby number reaches $\mathcal{O}(1)$, geostrophic balance is lost and a vertical secondary ageostrophic circulation begins to slump the isopycnals and restore the flow to a more geostrophically-balanced flow. This ageostrophic secondary circulation therefore generates “hot spots” of higher vertical velocities. The fine-scale structures in the vertical velocity field corresponding to $\mathcal{O}(1)$ Rossby numbers can be seen in Figure 5, with local vertical velocities up to 60 m/day ($\sim 7 \times 10^{-4}$ m/s). Contrary to the PDF of relative vorticity, the distribution of vertical velocities demonstrate a negative skewness ($s = -0.25$). This is in agreement with the theory: In fact, positive relative vorticity is associated with the dense side of a density front, where vertical velocities are negative (Mahadevan, 2016). Once again, the amplitude of these vertical velocity hot spots is coherent with the scaling $w \propto Ro f U / N$: using $Ro \sim 1$, $N \sim 10^{-2}$ 1/s, $f \sim 10^{-5}$ 1/s, and $U \sim 0.1$ m/s, we obtain $w \sim 10^{-4}$ m/s, or $\sim 10^1$ m/day.

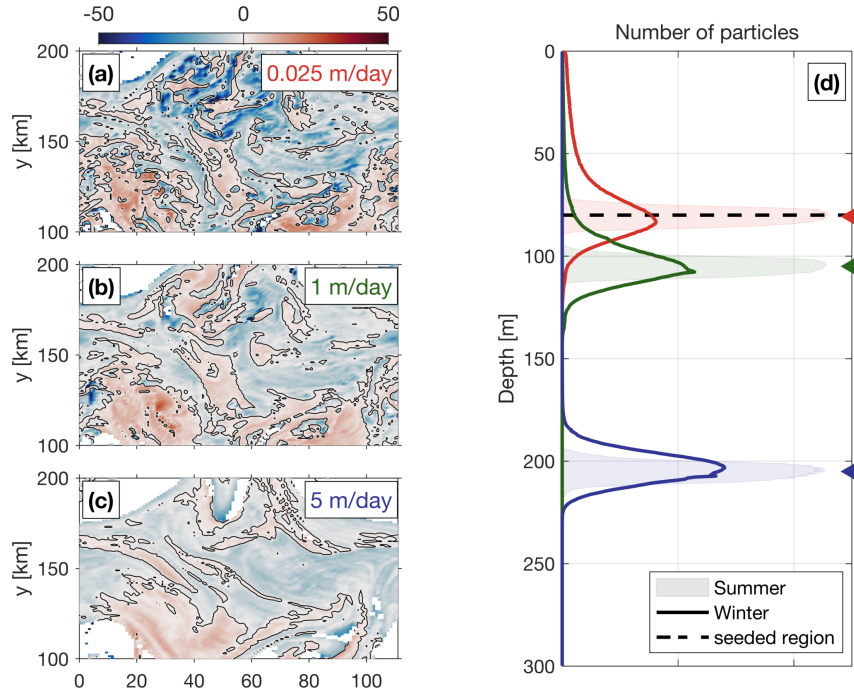
Comparing *Papa-summer* and *Papa-winter* highlights the different dynamical regimes in the two experiments. In *Papa-winter*, density fronts tend to be sharper, meaning larger density gradients over shorter spatial scales. When computed at the kilometer-scale, the PDF of horizontal buoyancy gradients in *Papa-winter* exhibits a longer tail than in *Papa-summer* (Figure 5). When compared to observations, the PDFs of M^2 in *Papa-summer* and *Papa-winter* demonstrate a correlation with observations of $r = 0.93$ and $r = 0.95$, respectively.

The wider PDF of vertical velocities in *Papa-winter* shows advective velocities that match and exceed typical gravitational sinking velocities, particularly for smaller, and therefore slower-sinking, particulate organic material. The secondary ageostrophic circulation that develops at submeso-scales (i.e., $Ro \mathcal{O}(1)$) therefore generates an export mechanism that directly competes with the traditional paradigm that relies on gravitational sinking leading the export of particulate matter in the ocean.

3.2 Gravitational and Advective Export of POC

Both model experiments described above were then used to investigate the relationship between ocean dynamics and particle downward flux, using Lagrangian particle-tracking. Domain-averaged, downward particle flux is expected to be a combination of the flux driving by gravitational sinking ($\langle w_s B \rangle$), and by the vertical advective currents affecting the particle along its pathway ($\langle wB \rangle$). The deviation in particle depths from the traditional one-dimensional gravitationally driven model is shown in Figure 6 for both summer and winter cases. In the summer, the PDF of particle density versus depth remains relatively narrow through time, and is centered on a depth level that can be predicted using a simple 1D gravitational model (see shaded curves in Figure 6). The spread in the particle density also vary little among particle classes with different sinking velocities, suggesting that downward fluxes of particles is greatly dominated by gravitational settling and is not subject to significant vertical ocean currents.

In the winter, however, PDFs of particle density versus depth is wider, in agreement with the stronger vertical ocean currents occurring in the winter (see Figure 5). A top-view of the deviation in the downward particle flux from the traditionally considered 1D gravitational model can be seen in Figure 6 (panels (a)-(c)). Slower-sinking particles deviate more than faster-sinking particles, exhibiting median depth anom-



457 **Figure 6.** [left] The median depth anomaly of particles with a sinking speed (a) 0.025 m/d,
458 (b) 1 m/d, (c) 5 m/d within each grid cell for the winter case 25 days after particles are released.
459 The ‘depth anomaly’ is with respect to the ‘expected’ sinking depth (= sinking speed \times time
460 since release). Blue (red) grid cells indicate that the median depth of particles in this cell is
461 deeper (shallower) than expected, based on a 1D gravitational model where $z = w_s \times t$. [right]
462 (d) Probability Distribution Function (PDF) of particles as a function of depth for each velocity
463 class. The winter distribution is shown as thick lines, while the summer distribution is repre-
464 sented by the shaded regions. Triangle markers indicate the expected depth of particles after 25
465 days based on the 1D gravitational model, which is used as a reference to compute the depth
466 anomalies. Release depth is indicated by the thick dashed line.

472 lies up to 50 m. This is due to the fact that slower-sinking particles spend more time
473 in the mixed layer, where most of the stronger vertical currents tend to occur (Figure
474 5). An interesting result emerges from the spatial distribution of the depth-anomaly:
475 both positive (i.e., particles are shallower than expected) and negative (i.e., particles
476 are deeper than expected) anomalies are organized into features with a length-scale
477 $\mathcal{O}(1\text{-}10 \text{ km})$. This further highlights the importance of winter submesoscale circulation
478 for vertical fluxes of particles.

479 A relative amount of biomass is associated to the particles using Equation (8).
480 PDFs of relative biomass as a function of the vertical velocity is shown in Figure 7.
481 Following the traditional paradigm derived from the simple 1D gravitational model, the
482 downward flux of biomass in the summer is dominated by faster-sinking particle classes
483 capable of carrying particulate material downwards more efficiently. The contribution
484 of slower-sinking particles, however, depends critically on the slope of the size spectrum
485 (see Figure 4). As the Junge slope increases, the spectrum of biomass steepens, and
486 the relative contribution of slower-sinking particles to the downward biomass flux
487 significantly increases (Figure 7c). In fact, the contribution of slower-sinking particles

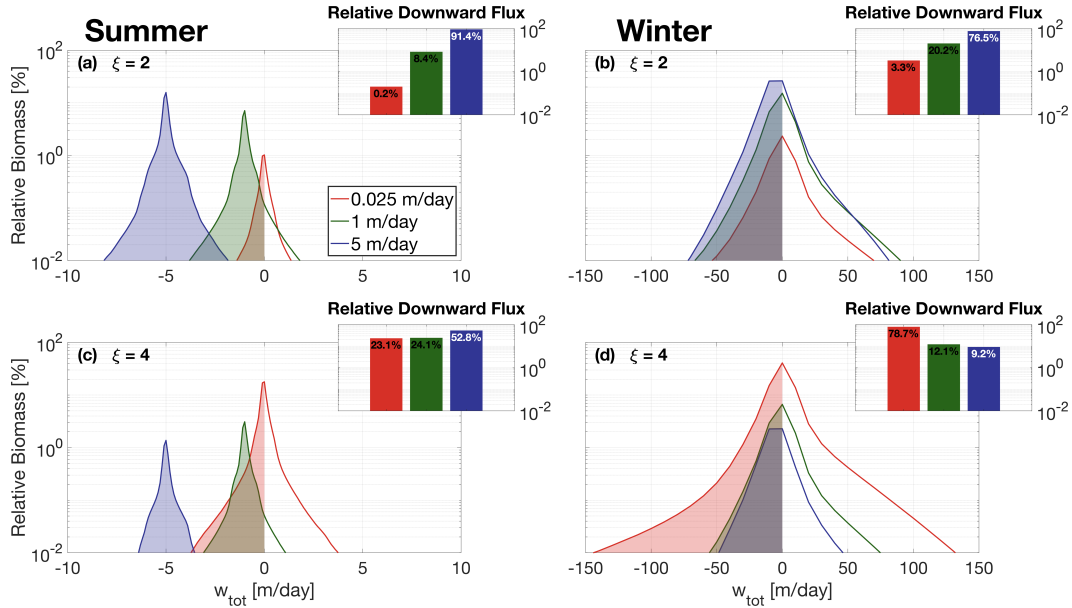


Figure 7. Probability Distribution Function (PDF) of relative biomass versus total vertical velocity ^{c3}(sinking + advective) along particle trajectories in the summer case [left] and winter case [right], with a Junge slope of 2 [top] and 4 [bottom]. ^{c4}PDFs are computed from the whole 24-day particle tracking experiments. Inserts show the integrated relative downward biomass flux associated with each sinking-velocity class, categorized according to their initial sinking velocity. Both winter dynamics and steeper Junge slopes tend to increase the relative contribution of slower-sinking particles.

to the summer downward flux increases by a factor 100 (from 0.2% to ^{c1}0%) when the Junge slope varies from $\xi = 2$ to $\xi = 4$. While significant, the impact of a change in the Junge slope in summer conditions does not challenge the dominant role played by faster-sinking particles. This result can be explained by the fact that, in the summer, vertical velocities are weak and vertical biomass fluxes are therefore gravitationally-driven ($\langle w_s B \rangle > \langle w B \rangle$).

In the winter, PDFs of relative biomass as a function of vertical velocities present a much larger spread, with velocity magnitudes exceeding 50 m/day. For $\xi = 2$, the relative contribution of slower-sinking particles to the downward flux significantly increases from 0.2% in the summer to about 3% in the winter, demonstrating the impact advective velocities alone can have on vertical fluxes (Figure 7b). Nevertheless, slower-sinking particles remain a relatively small contributor to the total downward flux of biomass. When winter ocean dynamics are coupled with a steeper Junge slope, however, slower-sinking particles largely dominate the downward biomass flux. In our winter simulations with $\xi = 4$, we find that the slowest-sinking particle class is responsible for about 79% of the biomass flux (Figure 7d).

Our results show that both a steepening of the particle size spectrum and the presence of submesoscale dynamics can enhance the contribution of slower-sinking particles to the downward biomass flux. While the former is simply due to an increase in particle density in slower-sinking particle classes, the latter is attributed to the larger

^{c1} ^{c2}

515 vertical velocity generated by submesoscale instabilities. When both are combined,
 516 as expected in the wintertime, slower-sinking particles then become the leading con-
 517 tributor to the downward biomass transport. However, slower-sinking particles are
 518 generally expected to remineralize on timescales shorter than their export timescale,
 519 fueling the argument that the focus should be upon faster-sinking particle classes. The
 520 impacts of remineralization on export are thus considered in the following section to
 521 test the robustness of the findings.

522 3.3 Particle Remineralization

523 Both submesoscale dynamics and the Junge slope were identified as key factors
 524 impacting the respective role played by different particle classes in driving downward
 525 biomass fluxes. Simple Lagrangian particles were used to isolate the effects of these
 526 two factors. In reality, however, sinking velocities of particulate matter varies in time
 527 as the particles slowly remineralize. A remineralizing behavior was therefore imple-
 528 mented for the Lagrangian particles, using Equation (10), to investigate the impact
 529 that remineralization processes have on our findings. The traditional paradigm relies
 530 on the fact that slow-sinking particles tend to fully remineralize over short timescales,
 531 further enhancing the importance of faster-sinking particles classes in driving down-
 532 ward biomass fluxes. While this paradigm holds for flatter Junge slope, where the
 533 biomass content is dominated by faster-sinking particles, it becomes unfit at steeper
 534 slopes.

535 Figure 8 compares the relative biomass and downward biomass fluxes associ-
 536 ated with each of the modeled particle classes for ^{c1} $\xi = 2$ and $\xi = 4$ ^{c2}including
 537 the remineralization scheme. As previously detailed, downward fluxes of biomass
 538 are dominated by faster-sinking particles during summertime and in the absence of
 539 remineralization ^{c3}(see Figure 7). This is due to the fact that the flux of biomass
 540 $\langle w_{tot}B \rangle = \langle w_s B \rangle + \langle w B \rangle$ is driven by $\langle w_s B \rangle$, despite a smaller relative biomass content
 541 per particle. This is characteristic of a gravitationally-driven system, where settling
 542 velocity dictates the contribution to downward fluxes. Implementing remineralization
 543 processes, however, directly affects the particle settling velocity which slows down as
 544 particles remineralize. This effect can ^{c4}particularly be seen in Figure 8^{c5}a and c,
 545 where PDFs of relative biomass per particle class are shifted towards weaker vertical
 546 velocities than in the absence of remineralization, as predicted by Equation (10). ^{c6}

548 In an advectively-driven system where $\langle w_s B \rangle \sim \langle w B \rangle$, the relative amount of
 549 biomass content in a particle class becomes important and dictates the respective con-
 550 tribution of each particle class to the total downward biomass fluxes. This shift from a
 551 gravitationally-driven to an advectively-driven system is observed when implementing
 552 particle remineralization in the summer (Figure 8^{c9}): in the absence of remineral-
 553 ization, faster-sinking particles dominate the downward biomass fluxes (^{c10}53%; see
 554 Figure 7c). When remineralization processes are considered, slower-sinking particles
 555 ^{c11}contribute more to biomass fluxes (see inset in Figure 8c). As shown in Figure 7,
 556 downward biomass fluxes in the wintertime are generally advectively-driven, due to the

^{c1} *Text added.*

^{c2} ~~with and without~~

^{c3} *Text added.*

^{c4} *Text added.*

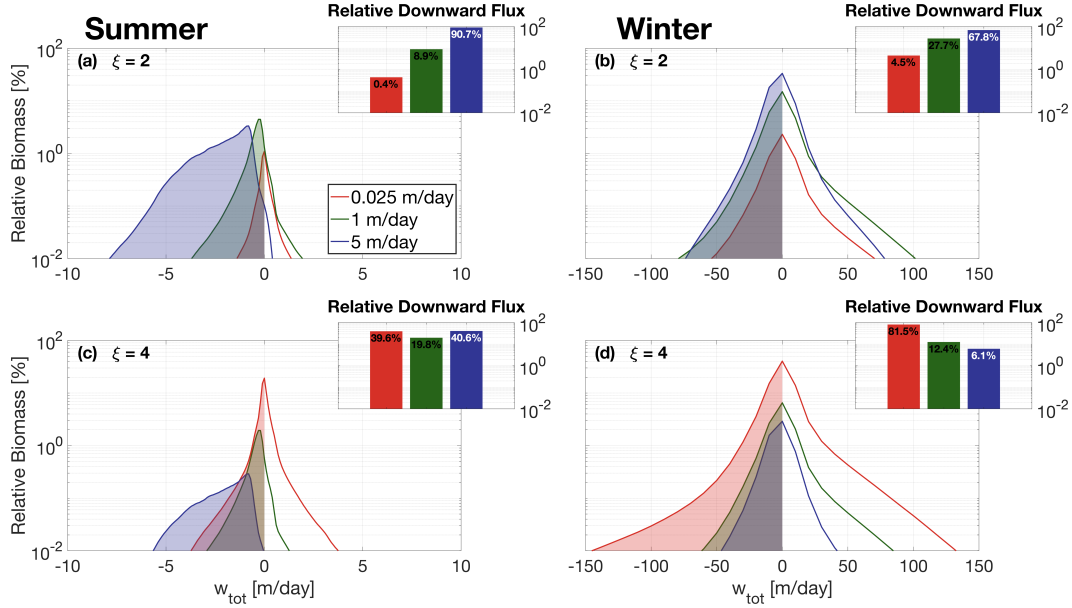
^{c5} *Text added.*

^{c6} ~~As a result, the gravitationally-driven term $\langle w_s B \rangle$ decreases with time, and the downward flux of biomass becomes generally advectively-driven by day 25 (Figure 8).~~

^{c9} e

^{c10} 60

^{c11} ~~become the dominant contributor~~



547 **Figure 8.** ^{c8}Same as Figure 7, but including particle remineralization (see Equation 10).

557 larger vertical velocities associated with wintertime ocean dynamics. Biomass fluxes
 558 are dominated by the slower-sinking particles ^{c12}when $\xi = 4$, representing 79% of the
 559 downward biomass flux (Figure 7d). Even after implementing the remineralization
 560 scheme, slower-sinking particles remain the largest contributor to downward biomass
 561 fluxes (82%; see Figure 8d).

562 These results highlight the importance in considering slower-sinking particle
 563 classes when considering downward biomass fluxes. It also demonstrates that, con-
 564 trarily to the traditional paradigm, remineralization processes enhance the role played
 565 by slower-sinking particles in biomass fluxes, in cases where the biomass spectrum
 566 slope is negative.

567 4 Discussion

568 4.1 Dynamical Regimes

569 *Papa-summer* and *Papa-winter* experiments were designed to statistically cap-
 570 ture the ocean dynamics at Station Papa (145°W , 50°N) in the Northeast Pacific
 571 Ocean. After spin-up, the model demonstrated similar distributions of both horizontal
 572 (M^2) and vertical (N^2) density gradients to observational estimates from underwater
 573 gliders (see Figures 2, 3, and 5). The two experiments, however, show significantly
 574 different distributions of M^2 , with the winter distribution exhibiting a longer tail, due
 575 to sharper density gradients. The tail of the wintertime distribution is only partially
 576 captured by the glider data, due to the fact that underwater gliders sampled gradients
 577 at spatial scales of 10 km and greater, while the model has a horizontal resolution of
 578 500 m, allowing sharper submesoscale fronts and filaments to be formed.

579 Studies investigating submesoscale dynamics traditionally focused on regions
 580 where the presence of submesoscale fronts and filaments are established, such as west-

^{c12} *Text added.*

ern boundary currents with strong gradients (D'Asaro, Lee, Rainville, Harcourt, & Thomas, 2011; Thomas, Tandon, & Mahadevan, 2013), or the edge of mesoscale features (van Haren et al., 2006; Waite et al., 2016). The seasonality in submesoscale dynamics captured in the glider dataset at Station Papa and reflected in the model experiments, echoes the behavior seen from recent observational studies conducted at a similar latitude in the Atlantic Ocean, which demonstrate the intensification of submesoscale dynamics in the wintertime (Buckingham et al., 2016; Thompson et al., 2016). Despite being sometimes qualified as an “eddy desert” with low kinetic energy (Chelton, Schlax, & Samelson, 2011), ocean characteristics in the eastern part of the Pacific subpolar gyre suggest the presence of submesoscale features in the wintertime: strong density gradients, localized Rossby numbers of order 1, a balanced Richardson number $Ri_b = \frac{f^2 N^2}{M^4}$ smaller than 1, a positively skewed distribution in vorticity, and a negatively skewed distribution of vertical velocities (see Figure 5; Buckingham et al., 2016; Rudnick, 2001; Thomas, Taylor, et al., 2013).

Strong downward velocities are hypothesized to enhance POC export by advecting slower-sinking particles out of the mixed layer. *Papa_winter* indeed exhibits vertical velocities more than 20 times larger than in *Papa_summer*. The vertical currents in *Papa_winter*, however, tend to be much patchier than the weaker vertical currents observed in *Papa_summer*. Because both particle production and downward vertical velocities present a high degree of patchiness, it requires a certain level of covariance between the two fields for the export to effectively be enhanced (Mahadevan et al., 2012). A more realistic seeding strategy for Lagrangian particles, such as one guided by biological tracers, would likely provide important information towards a better understanding of the effects of patchiness on POC export at submeso-scales

The hypothesis tested in this study is that submesoscale activity enhances export of particulate matter at Station Papa by shortening the export timescale of particulate matter. The wintertime intensification in submesoscale activity has the potential to indeed enhance export (see discussion in Section 4.2). However, the seasonal cycle in submesoscale activity is out of phase with the one in net community productivity, which peaks in the spring and summertime when the mixed layer is shallower (Plant et al., 2016). Two mechanisms are therefore present to potentially sustain a year-long POC export flux: In the winter, less particulate material is present in the mixed layer, but active submesoscale dynamics tend to enhance the POC export flux by advecting the more numerous slower-sinking particles into the ocean interior. In the summer, the production of POC is at its yearly maximum, but export tends to be dominated by gravitational sinking, which favors faster-sinking particles and thus exclude part of the particle spectrum from contributing to the export flux.

4.2 Downward Fluxes

Analyses of particle tracking experiments reveal that the contribution of slower-sinking particles to the downward particulate flux depends on two main factors: (1) the dynamics of the oceanic flow field, and (2) the slope of the size spectrum (i.e., the Junge slope ξ).

Mixed layer ocean dynamics at station Papa change significantly between the winter and the summer. In the winter, submesoscale dynamics are intensified, and sharp fronts and filaments develop in the mixed layer. This seasonal change in dynamics is consistent with recent observations (Buckingham et al., 2016; Thompson et al., 2016), and models (Brannigan, Marshall, Naveira-Garabato, & George Nurser, 2015; Callies et al., 2015; Rocha, Gille, Chereskin, & Menemenlis, 2016) characterizing the seasonal cycle of submesoscale dynamics. The winter intensification in submesoscale dynamics was proven to have an important impact on the downward flux of all sinking-velocity classes modeled in this experiment.

632 In the summer, gravitational sinking governs a downward particulate flux, which
 633 is dominated by faster-sinking particles, with little to no contribution from slower-
 634 sinking particles. In the winter, however, vertical fluxes tend to be advectively-driven,
 635 which leads to a slightly weaker downward flux of faster-sinking particles than in the
 636 summer due to resuspension, but a much larger flux of slower-sinking particles, which
 637 are present in far greater numbers (Figure 7). The gravitationally-driven flux in the
 638 summer is mechanistically different from the advectively-driven winter flux, which
 639 raises the question as to which process is most efficient in driving a downward flux of
 640 particulate material.

641 In the absence of remineralization, both a steeper size spectrum slope ($\xi > 3$ in
 642 this case) and enhanced submesoscale dynamics, increase the contribution of slower-
 643 sinking particle classes to the downward biomass flux. This is only when both of
 644 these conditions are combined, however, that slower-sinking particles dominate the
 645 downward flux of biomass (Figure 7). This is a significant result, as Junge slopes
 646 greater than 3 have been observed in the ocean ^{c1}: In-situ observations yield aver-
 647 age spectral slopes varying between 3.5 and 4.5 (Kostadinov, Siegel, & Maritorena,
 648 2009, see Table 2 in)^{c2}, while spectral analysis of satellite data suggest global spectral
 649 slopes varying between 3 and 6. More recent observational work located in the North-
 650 east Pacific, including Station Papa, found a spectral slope also greater than 3 (White
 651 et al., 2015, ; Z. Xiaodong, personal communication). ^{c3}Junge slopes are expected to
 652 vary in space, depending on the community composition, both lateraly and vertically
 653 (Kostadinov et al., 2009; White et al., 2015)^{c4}, as well as in time; spectrum slopes
 654 tend to be flatter during a spring bloom event, where larger particles (e.g., diatoms)
 655 are produced in large quantities, and steeper during the wintertime, when commu-
 656 nities are mostly composed of small particles. The threshold value of $\xi = 3$ for a
 657 change in the biomass spectral slope (see Figure 4b) is of course a consequence of first-
 658 order approximations used in this study describing the relationships between particle
 659 size, sinking velocity, and biomass content. Nevertheless, our results demonstrate the
 660 importance of including the smaller particle size range of the particle spectrum, in the
 661 estimation or measurement of vertical fluxes, especially when submesoscale dynamics
 662 are active. It also highlights the importance of better constraining the relationships
 663 linking particle size, sinking velocity, and biomass content.

664 Introducing remineralization processes significantly decreases the biomass flux.
 665 Counter-intuitively, however, the implementation of a remineralization scheme further
 666 strengthens the contribution of slower-sinking particles to the biomass flux (Figure
 667 8). This can be explained by the fact that remineralization processes have a greater
 668 impact on sinking-velocity classes that rely on gravitational sinking to be exported, as
 669 these particles decelerate as they remineralize. In the summer, all particle classes are
 670 similarly affected by remineralization, as downward fluxes are gravitationally-driven.
 671 In the winter, however, slower-sinking particles are exported through advective pro-
 672 cesses. Their export timescale is barely affected by remineralization processes as it
 673 only depends on local ocean dynamics.

674 ^{c5}These results are robust to the range of sinking rates explored. If one considers
 675 a particle class with a sinking rate far exceeding the vertical advective velocity (e.g.,
 676 100 m/day; Turner, 2015)^{c6}, then the associated biomass flux can be estimated by
 677 relying on the traditional 1-D paradigm, assuming $w_{tot} \approx w_s$. Combining this approx-

^{c1} Text added.

^{c2} Text added.

^{c3} Text added.

^{c4} Text added.

^{c5} Text added.

^{c6} Text added.

imation with Equation 8 shows that the slope of the biomass flux spectrum is positive for $\xi < 5$, in which case very fast-sinking particles would dominate vertical biomass fluxes. However, for $\xi > 5$, the slope of the biomass flux spectrum becomes negative as well, meaning that the biomass flux is always dominated by the slow-sinking particle classes, regardless of the ocean dynamical regime. While considered large, values of $\xi > 5$ remain realistic and fall within the range obtained from satellite-based estimates (Kostadinov et al., 2009).

The results of this study suggest that slow- and non-sinking particles must be considered when studying the downward flux of particulate matter in the upper ocean. The patchiness associated with both particle production and submesoscale features poses a real observational challenge to properly resolve vertical fluxes. Based on our findings, subsequent studies should focus on testing the impact of patchiness on vertical fluxes. In the wintertime, when size spectral slope is steep and submesoscale dynamics most active, vertical fluxes could be grossly underestimated depending on the level of co-occurrence between particle production and stronger vertical currents.

5 Conclusion

The main conclusions of this study are:

1. Ocean dynamics in the subpolar Northeast Pacific exhibit a seasonal cycle with low submesoscale activity in the summertime, and more submesoscale features present in the wintertime. Submesoscale dynamics generate larger, and asymmetric, vertical currents leading to a vertical biomass flux driven by advective processes, as opposed to gravitational sinking in the summertime.
2. Submesoscale dynamics generally enhance the downward particulate flux by increasing the contribution of slower-sinking particles to the total flux through advective transport. The slower-sinking particles are found to be significant for export, and can be even make the dominant contribution under certain conditions.
3. The contribution of slower-sinking particles to the downward biomass flux depends on the slope of the particle size spectra (i.e., the Junge Slope), that controls the relative number of particles per size class. Two cases emerge from this study:
 - (a) If the Junge slope is smaller than 3, larger particles contribute most to vertical biomass fluxes independently of flow dynamics, as there are no mechanisms capable of selectively advecting slower-sinking particles. The system is described as gravitationally-driven.
 - (b) If the Junge slope is greater than 3, as most commonly observed, ocean dynamics become key for determining which particle classes dominate the downward flux. As submesoscale dynamics become more active, ageostrophic circulations leading to larger vertical velocities develop. In these conditions, downward biomass fluxes are largely driven by the slower-sinking particle classes.
4. Remineralization processes logically reduce the amount of biomass flux. However, it unexpectedly enhances the role of slower-sinking particles, which are advectively transported. The impact of remineralization is greater on faster-sinking particles since it affects both the biomass content and their sinking velocity.

724 Acknowledgments

725 The work was funded by NASA grant NNX16AR48G, to complement the EXport
 726 Processes in the global Ocean from RemoTe Sensing (EXPORTS) program. We would
 727 like to thank A. Thompson (Caltech) for his useful comments and suggestions, N.
 728 Pelland (NOAA) and C. Eriksen (University of Washington) for sharing the glider data
 729 collected at Ocean Station Papa, as well as S. Essink for his assistance in developing the
 730 particle-tracking code. All data used in this manuscript are publicly available: Ocean
 731 Station Papa data is available on PMEL's website (<https://www.pmel.noaa.gov/ocs/Papa>; PMEL, 2018) and gridded Argo products can be downloaded at <http://www.seanoe.org/data/00348/45945> (Gaillard, 2015). Glider data is archived at the
 732 University of Washington's Library (<http://hdl.handle.net/1773/41656>; Pelland,
 733 2018).

734

735

736 References

- 737 Alkire, M., D'Asaro, E., Lee, C., Perry, M., Gray, A., Cetinic, I., ... González-
 738 Posada, A. (2012). Estimates of net community production and export using
 739 high-resolution, Lagrangian measurements of O₂, NO₃⁻, and POC through the
 740 evolution of a spring diatom bloom in the North Atlantic. *Deep-Sea Res. I*,
 741 64, 157-174. doi: 10.1016/j.dsr.2012.01.012
- 742 Bach, L. T., Riebesell, U., Sett, S., Febiri, S., Rzepka, P., & Schulz, K. G. (2012).
 743 An approach for particle sinking velocity measurements in the 3400 μm size
 744 range and considerations on the effect of temperature on sinking rates. *Marine
 745 Biology*, 159(8), 1853–1864. doi: 10.1007/s00227-012-1945-2
- 746 Bower, A. S., & Rossby, T. (1989). Evidence of Cross-Frontal Exchange Processes
 747 in the Gulf Stream Based on Isopycnal RAFOS Float Data. *Journal of Phys-
 748 ical Oceanography*, 19(9), 1177–1190. doi: 10.1175/1520-0485(1989)019<1177:
 749 EOCFEP>2.0.CO;2
- 750 Brannigan, L., Marshall, D. P., Naveira-Garabato, A., & George Nurser, A. (2015).
 751 The seasonal cycle of submesoscale flows. *Ocean Modelling*, 92, 69–84. doi: 10
 752 .1016/j.ocemod.2015.05.002
- 753 Briggs, N., Perry, M. J., Cetini, I., Lee, C., D'Asaro, E., Gray, A. M., & Rehm, E.
 754 (2011). High-resolution observations of aggregate flux during a sub-polar north
 755 atlantic spring bloom. *Deep Sea Research Part I: Oceanographic Research
 756 Papers*, 58(10), 1031 - 1039. doi: 10.1016/j.dsr.2011.07.007
- 757 Buckingham, C. E., Naveira Garabato, A. C., Thompson, A. F., Brannigan, L.,
 758 Lazar, A., Marshall, D. P., ... Belcher, S. E. (2016). Seasonality of sub-
 759 mesoscale flows in the ocean surface boundary layer. *Geophysical Research
 760 Letters*, 43(5), 2118–2126. doi: 10.1002/2016GL068009
- 761 Callies, J., Ferrari, R., Klymak, J. M., & Gula, J. (2015). Seasonality in sub-
 762 mesoscale turbulence. *Nature communications*, 6, 6862. doi: 10.1038/
 763 ncomms7862
- 764 Chelton, D. B., Schlax, M. G., & Samelson, R. M. (2011). Global observations of
 765 nonlinear mesoscale eddies. *Progress in Oceanography*, 91(2), 167–216. doi: 10
 766 .1016/j.pocean.2011.01.002
- 767 D'Asaro, E., Lee, C., Rainville, L., Harcourt, R., & Thomas, L. (2011). Enhanced
 768 turbulence and energy dissipation at ocean fronts. *Science*, 332(6027), 318–
 769 322. doi: 10.1126/science.1201515
- 770 Döös, K., Kjellsson, J., & Jönsson, B. (2013). TRACMASS – A Lagrangian Trajec-
 771 tory Model. In *Preventive methods for coastal protection* (pp. 225–249). Heidel-
 772 berg: Springer International Publishing. doi: 10.1007/978-3-319-00440-2_7
- 773 Ducklow, H. W., Steinberg, D. K., & Buesseler, K. O. (2001). Upper Ocean Carbon
 774 Export and the Biological Pump. *Oceanography*, 14. doi: <https://doi.org/10.5670/oceanog.2001.06>
- 775

- 776 Estapa, M. L., Siegel, D. A., Buesseler, K. O., Stanley, R. H. R., Lomas, M. W., &
 777 Nelson, N. B. (2015). Decoupling of net community and export production
 778 on submesoscales in the Sargasso Sea. *Global Biogeochemical Cycles*, 29(8),
 779 1266–1282. doi: 10.1002/2014GB004913
- 780 Falkowski, P. G., Barber, R. T., & Smetacek, V. (1998). Biogeochemical Controls
 781 and Feedbacks on Ocean Primary Production. *Science*, 281(5374), 200–206.
 782 doi: 10.1126/science.281.5374.200
- 783 Fox-Kemper, B., Ferrari, R., & Hallberg, R. (2008). Parameterization of Mixed
 784 Layer Eddies. Part I: Theory and Diagnosis. *Journal of Physical Oceanogra-*
 785 *phy*, 38(6), 1145–1165. doi: 10.1175/2007JPO3792.1
- 786 Gaillard, F. (2015). ISAS-13 temperature and salinity gridded fields. SEANOE. doi:
 787 10.17882/45945
- 788 Gaillard, F., Reynaud, T., Thierry, V., Kolodziejczyk, N., & von Schuckmann, K.
 789 (2016). In situ-based reanalysis of the global ocean temperature and salinity
 790 with isas: Variability of the heat content and steric height. *Journal of Climate*,
 791 29(4), 1305–1323. doi: 10.1175/JCLI-D-15-0028.1
- 792 Gruber, N., Lachkar, Z., Frenzel, H., Marchesiello, P., Münnich, M., McWilliams,
 793 J. C., ... Plattner, G.-K. (2011). Eddy-induced reduction of biological pro-
 794 duction in eastern boundary upwelling systems. *Nature geoscience*, 4(11), 787.
 795 doi: 10.1038/NGEO1273
- 796 Harrison, P. J., Whitney, F. A., Tsuda, A., Saito, H., & Tadokoro, K. (2004).
 797 Nutrient and Plankton Dynamics in the NE and NW Gyres of the Sub-
 798 arctic Pacific Ocean. *Journal of Oceanography*, 60(1), 93–117. doi:
 799 10.1023/B:JOCE.0000038321.57391.2a
- 800 Hoskins, B. J., & Bretherton, F. P. (1972). Atmospheric Frontogenesis Models:
 801 Mathematical Formulation and Solution. *Journal of the Atmospheric Sciences*,
 802 29(1), 11–37. doi: 10.1175/1520-0469(1972)029<0011:AFMMFA>2.0.CO;2
- 803 Iversen, M. H., & Ploug, H. (2010). Ballast minerals and the sinking carbon flux in
 804 the ocean: carbon-specific respiration rates and sinking velocity of marine snow
 805 aggregates. *Biogeosciences*, 7(9), 2613–2624. doi: 10.5194/bg-7-2613-2010
- 806 Iversen, M. H., & Ploug, H. (2013). Temperature effects on carbon-specific respi-
 807 ration rate and sinking velocity of diatom aggregates - potential implications
 808 for deep ocean export processes. *Biogeosciences*, 10(6), 4073–4085. doi:
 809 10.5194/bg-10-4073-2013
- 810 Klein, P., & Lapeyre, G. (2009). The Oceanic Vertical Pump Induced by Mesoscale
 811 and Submesoscale Turbulence. *Annual Review of Marine Science*, 1(1), 351–
 812 375. doi: 10.1146/annurev.marine.010908.163704
- 813 Kostadinov, T. S., Siegel, D. A., & Maritorena, S. (2009). Retrieval of the particle
 814 size distribution from satellite ocean color observations. *Journal of Geophysical*
 815 *Research*, 114(C9), C09015. doi: 10.1029/2009JC005303
- 816 Lévy, M., Ferrari, R., Franks, P. J. S., Martin, A. P., & Rivière, P. (2012). Bringing
 817 physics to life at the submesoscale. *Geophysical Research Letters*, 39(14), n/a–
 818 n/a. doi: 10.1029/2012GL052756
- 819 Lévy, M., Klein, P., & Treguier, A.-M. (2001). Impact of sub-mesoscale physics on
 820 production and subduction of phytoplankton in an oligotrophic regime. *Jour-*
 821 *nal of marine research*, 59(4), 535–565. doi: 10.1357/002224001762842181
- 822 Mahadevan, A. (2016). The Impact of Submesoscale Physics on Primary Produc-
 823 tivity of Plankton. *Annual Review of Marine Science*, 8(1), 161–184. doi: 10
 824 .1146/annurev-marine-010814-015912
- 825 Mahadevan, A., & Archer, D. (2000). Modeling the impact of fronts and
 826 mesoscale circulation on the nutrient supply and biogeochemistry of the up-
 827 per ocean. *Journal of Geophysical Research: Oceans*, 105(C1), 1209–1225. doi:
 828 10.1029/1999JC900216
- 829 Mahadevan, A., D'Asaro, E., Lee, C., & Perry, M. J. (2012). Eddy-Driven Strat-
 830 ification Initiates North Atlantic Spring Phytoplankton Blooms. *Science*,

- 831 337(6090), 54–58. doi: 10.1126/science.1218740
- 832 Mahadevan, A., Olinger, J., & Street, R. (1996a). A Nonhydrostatic Mesoscale Ocean
833 Model. Part II: Numerical Implementation. *Journal of Physical Oceanography*,
834 26(9), 1881–1900. doi: 10.1175/1520-0485(1996)026<1881:ANMOMP>2.0.CO;
835 2
- 836 Mahadevan, A., Olinger, J., & Street, R. (1996b). A Nonhydrostatic mesoscale ocean
837 model. Part I: Well-posedness and scaling. *Journal of Physical Oceanography*,
838 26(9), 1868–1880. doi: 10.1175/1520-0485(1996)026<1868:ANMOMP>2.0.CO;
839 2
- 840 Mahadevan, A., & Tandon, A. (2006). An analysis of mechanisms for submesoscale
841 vertical motion at ocean fronts. *Ocean Modelling*, 14(3-4), 241–256. doi: 10
842 .1016/J.OCEMOD.2006.05.006
- 843 McDonnell, A. M. P., & Buesseler, K. O. (2010). Variability in the average sinking
844 velocity of marine particles. *Limnology and Oceanography*, 55(5), 2085–2096.
845 doi: 10.4319/lo.2010.55.5.2085
- 846 McWilliams, J. C. (2016). Submesoscale currents in the ocean. *Proceedings of the
847 Royal Society A: Mathematical, Physical and Engineering Science*, 472(2189).
848 doi: 10.1098/rspa.2016.0117
- 849 Mensa, J. A., Garraffo, Z., Griffa, A., Özgökmen, T. M., Haza, A., & Veneziani, M.
850 (2013). Seasonality of the submesoscale dynamics in the Gulf Stream region.
851 *Ocean Dynamics*, 63(8), 923–941. doi: 10.1007/s10236-013-0633-1
- 852 Mesinger, F., DiMego, G., Kalnay, E., Mitchell, K., Shafran, P. C., Ebisuzaki, W.,
853 ... Shi, W. (2006). North american regional reanalysis. *Bulletin of the Ameri-
854 can Meteorological Society*, 87(3), 343–360. doi: 10.1175/BAMS-87-3-343
- 855 Omand, M. M., D'Asaro, E. A., Lee, C. M., Perry, M. J., Briggs, N., Cetini, I.,
856 & Mahadevan, A. (2015). Eddy-driven subduction exports particulate or-
857 ganic carbon from the spring bloom. *Science*, 348(6231), 222–225. doi:
858 10.1126/science.1260062
- 859 Pelland, N. (2018). *Seaglider Surveys at Ocean Station Papa: Bin-Averaged Profiles,
860 Currents, and Independent Oxygen Data*. Retrieved from [http://hdl.handle
861 .net/1773/41656](http://hdl.handle.net/1773/41656)
- 862 Pelland, N., Eriksen, C., & Cronin, M. (2016). Seaglider surveys at Ocean Station
863 Papa: Circulation and watermass properties in a meander of the North Pa-
864 cific Current. *Journal of Geophysical Research: Oceans*, 121, 6816–6846. doi:
865 10.1002/2016JC011920
- 866 Plant, J. N., Johnson, K. S., Sakamoto, C. M., Jannasch, H. W., Coletti, L. J.,
867 Riser, S. C., & Swift, D. D. (2016). Net community production at Ocean Sta-
868 tion Papa observed with nitrate and oxygen sensors on profiling floats. *Global
869 Biogeochemical Cycles*, 30(6), 859–879. doi: 10.1002/2015GB005349
- 870 Ploug, H., Iversen, M. H., Koski, M., & Buitenhuis, E. T. (2008). Production,
871 oxygen respiration rates, and sinking velocity of copepod fecal pellets: Direct
872 measurements of ballasting by opal and calcite. *Limnology and Oceanography*,
873 53(2), 469–476. doi: 10.4319/lo.2008.53.2.0469
- 874 PMEL. (2018). *Pacific Marine Environment Laboratory Ocean Climate Sta-
875 tions Mooring Data*. Retrieved from [https://www.pmel.noaa.gov/ocs/
data-overview](https://www.pmel.noaa.gov/ocs/
876 data-overview)
- 877 Rocha, C. B., Gille, S. T., Chereskin, T. K., & Menemenlis, D. (2016). Seasonal-
878 ity of submesoscale dynamics in the Kuroshio Extension. *Geophysical Research
879 Letters*, 43(21), 11,304–11,311. doi: 10.1002/2016GL071349
- 880 Rudnick, D. L. (2001). On the skewness of vorticity in the upper ocean. *Geophysical
881 Research Letters*, 28(10), 2045–2048. doi: 10.1029/2000GL012265
- 882 Sheldon, R., Prakash, A., & Sutcliffe, W., Jr. (1972). The size distribution of parti-
883 cles in the ocean. *Limnology and Oceanography*, 17(3), 327–340. doi: 10.4319/
884 lo.1972.17.3.0327
- 885 Sherry, N. D., Boyd, P. W., Sugimoto, K., & Harrison, P. J. (1999). Seasonal and

- 886 spatial patterns of heterotrophic bacterial production, respiration, and biomass
887 in the subarctic NE Pacific. *Deep-Sea Research Part II: Topical Studies in*
888 *Oceanography*, 46(11-12), 2557–2578. doi: 10.1016/S0967-0645(99)00076-4
- 889 Thomas, L. N., Tandon, A., & Mahadevan, A. (2013). Submesoscale processes and
890 dynamics. In *Ocean modeling in an eddying regime* (p. 17-38). American Geo-
891 physical Union (AGU). doi: 10.1029/177GM04
- 892 Thomas, L. N., Taylor, J. R., Ferrari, R., & Joyce, T. M. (2013). Symmetric in-
893 stability in the Gulf Stream. *Deep Sea Research Part II: Topical Studies in*
894 *Oceanography*, 91, 96–110. doi: 10.1016/j.dsr2.2013.02.025
- 895 Thompson, A. F., Lazar, A., Buckingham, C., Naveira Garabato, A. C., Damerell,
896 G. M., & Heywood, K. J. (2016). Open-Ocean Submesoscale Motions: A Full
897 Seasonal Cycle of Mixed Layer Instabilities from Gliders. *Journal of Physical*
898 *Oceanography*, 46(4), 1285–1307. doi: 10.1175/JPO-D-15-0170.1
- 899 Turner, J. T. (2015). Zooplankton fecal pellets, marine snow, phytodetritus and the
900 oceans biological pump. *Progress in Oceanography*, 130, 205–248.
- 901 van Haren, H., Millot, C., & Taupier-Letage, I. (2006). Fast deep sinking in Mediter-
902 ranean eddies. *Geophysical Research Letters*, 33(4), L04606. doi: 10.1029/
903 2005GL025367
- 904 Waite, A. M., Stemmann, L., Guidi, L., Calil, P. H. R., Hogg, A. M. C., Feng, M.,
905 ... Gorsky, G. (2016). The wineglass effect shapes particle export to the deep
906 ocean in mesoscale eddies. *Geophysical Research Letters*, 43(18), 9791–9800.
907 doi: 10.1002/2015GL066463
- 908 White, A. E., Letelier, R. M., Whitmire, A. L., Barone, B., Bidigare, R. R., Church,
909 M. J., & Karl, D. M. (2015). Phenology of particle size distributions
910 and primary productivity in the North Pacific subtropical gyre (Station
911 ALOHA). *Journal of Geophysical Research: Oceans*, 120(11), 7381–7399.
912 doi: 10.1002/2015JC010897